Ultrastructural, material and crystallographic description of endophytic masses – a possible damage response in shark and ray tessellated calcified cartilage

.
.
.
.
.
.
.

? Ymk cf Xg:

-
u
o
o
U
#

Ultrastructural, material and crystallographic description of endophytic masses – a possible damage response in shark and ray tessellated calcified cartilage

Ronald Seidel[1], Michael Blumer[2], Paul Zaslansky[3,4], David Knötel[5], Daniel R. Huber[6], James C. Weaver[7], Peter Fratzl[1], Sidney Omelon[1,8], Luca Bertinetti[1], Mason N. Dean[1]

[1] Department Biomaterials, Max Planck Institute of Colloids & Interfaces, Potsdam, Germany;

[2] Division of Clinical and Functional Anatomy, Medical University of Innsbruck, Innsbruck, Austria;

[3] Julius Wolff Institute, Charité - Universitätsmedizin Berlin, Germany;

[4] Department for Restorative and Preventive Dentistry, Charité - Universitätsmedizin Berlin, Germany;

[5] Department Visualization and Data Analysis, Zuse Institute Berlin, Germany;

[6] Department of Biology, University of Tampa, 401 W. Kennedy Blvd, Tampa, FL 33606, USA

[7] Wyss Institute for Biologically Inspired Engineering, Harvard University, Cambridge, MA, USA;

[8] Department of Chemical and Biological Engineering, University of Ottawa, Canada

ABSTRACT

The cartilaginous endoskeletons of Elasmobranchs (sharks and rays) are reinforced superficially by minute, mineralized tiles, called tesserae. Unlike the bony skeletons of other vertebrates, elasmobranch skeletons have limited healing capability and their tissues' mechanisms for avoiding damage or managing it when it does occur are largely unknown. Here we describe an aberrant type of mineralized elasmobranch skeletal tissue called endophytic masses (EPMs), which grow into the uncalcified cartilage of the skeleton, but exhibit a strikingly different morphology compared to tesserae and other elasmobranch calcified tissues. We use biological and materials characterization techniques, including computed tomography, electron and light microscopy, x-ray and Raman spectroscopy and histology to characterize the morphology, ultrastructure and chemical composition of tesserae-associated EPMs in different elasmobranch species. EPMs appear to develop between and in intimate association with tesserae, but lack the lines of periodic growth and varying mineral density characteristic of tesserae. EPMs are mineral-dominated (high mineral and low organic content), comprised of birefringent bundles of large monetite or brushite crystals aligned end to end in long strings. Both

tesserae and EPMs appear to develop in a type-2 collagen-based matrix, but in contrast to tesserae, all chondrocytes embedded or in contact with EPMs are dead and mineralized. The differences outlined between EPMs and tesserae demonstrate them to be distinct tissues. We discuss several possible reasons for EPM development, including tissue reinforcement, repair, and disruptions of mineralization processes, within the context of elasmobranch skeletal biology as well as descriptions of damage responses of other vertebrate mineralized tissues.

INTRODUCTION

The endoskeletons of sharks and rays (elasmobranch fishes) are typically described as being composed of unmineralized cartilage and two distinct types of calcified cartilage, which differ in their location and ultrastructure. Areolar calcified cartilage is a highly cellular, net-like mineralized tissue, with the cells occupying the holes in the net, that is only found in the centra of the vertebral column (Clement, 1992; Compagno 1988; Huber et al., 2013; Porter et al., 2006). In contrast, tessellated calcified cartilage comprises the remainder and vast majority of the endoskeleton (Fig. 1A-C) (Clement, 1992; Dean & Summers, 2006; Kemp et al., 1979; Seidel et al., 2016). Tessellated cartilage is a composite tissue, the primary skeletal material being an unmineralized, hyaline-like cartilage, covered in a thin rind of abutting calcified tiles, polygonal in shape and a few hundred microns in size, called tesserae. On top of this tessellated layer lies a fibrous tissue (perichondrium) surrounding or wrapping up the entire skeletal element (Fig. 1B,D). Tessellated cartilage has received the majority of research attention, and represents both a unique skeletal feature among vertebrates and a defining feature of the elasmobranch group for more than 400 million years (Long, 2015; Maisey, 2013).

Several additional, but uncommon calcified tissues have been described to date for elasmobranchs, all of which appear to be modifications of tessellated calcified cartilage, but far less universal in their distribution, being found only in specific parts of the body and/or phylogenetic groups (for summaries of these see Dean, 2011; Dean et al., 2015; Maisey, 2013). For example, the skeletons of the rostra of modern lamnid sharks and large extinct sclerorhynchid batoids are covered with exceptionally tall "columnar" tesserae which, in sclerorhynchids, can exhibit a mineralized overlay apparently formed from a mineralization of the perichondrium and obliteration of intertesseral spaces (Fig. 2A-C) (Compagno, 1988; Maisey, 2013; Mollen et al., 2012).

The long and slender saws of sawfishes, the jaws of hard prey-eating myliobatiform stingrays and the jaws of a variety of large shark species all are characterized by supranumerary tesseral layers, a thickening of the skeletal cortex via stacking of multiple tessellated layers (Fig. 2D-F) (Dean et al., 2006; Dingerkus et al., 1991; Summers, 2000).

In addition, in many elasmobranch taxa, but most pronounced in the jaws of myliobatiform stingrays, the skeleton can be further reinforced with trabecular cartilage, where tessellated struts pass through the uncalcified cartilage from one side of the jaw to the other (Fig. 2F) (Dean et al., 2006; Summers, 2000).
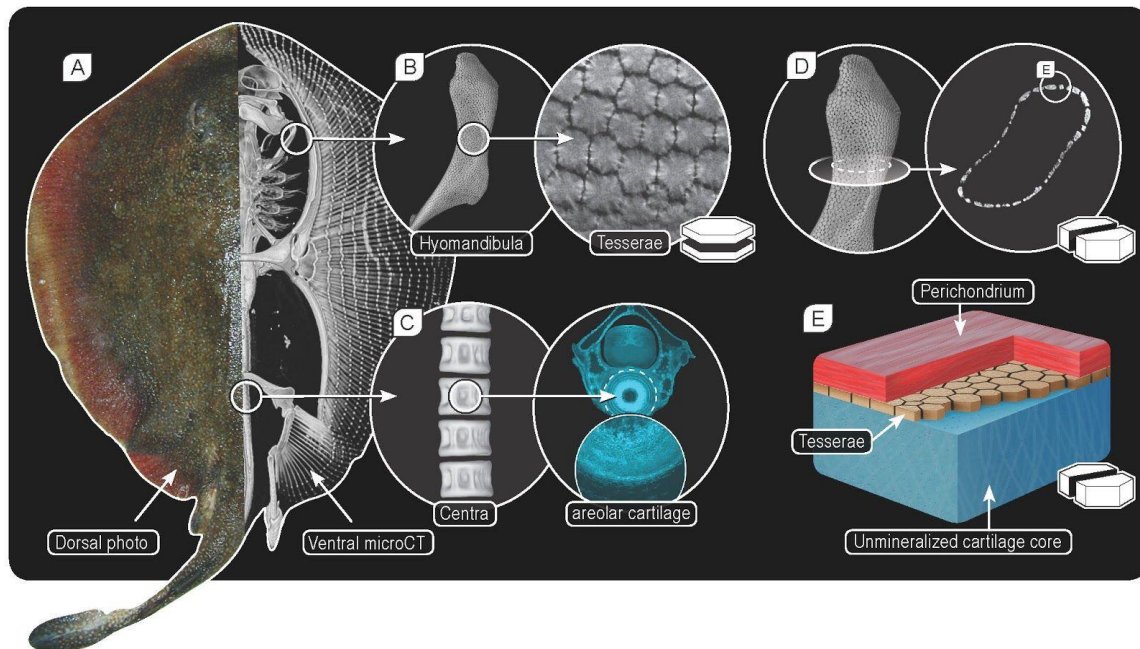

Figure 1. Calcified cartilage in the endoskeleton of elasmobranchs (sharks and rays).
A) Photograph of round stingray *Urobatis halleri* (left), and CT image (right) showing most of the skeleton is mineralized (and therefore visible using micro-computed tomography). Two major types of calcified cartilage are described in elasmobranchs: **B**) tessellated calcified cartilage consisting of individually mineralized tiles called tesserae (shown here in planar view), covering each skeletal elements' surface and **C**) areolar calcified cartilage located in the centre of the vertebrae. **D**) In cross sections of skeletal elements (here the hyomandibula), tesserae can be seen in vertical view. The section plane and orientation of the samples and images presented in this study are indicated by two icons; each a single schematic tessera sectioned either in planar or vertical view (inset B and D, respectively). **E**) General organization of the tissues forming elasmobranchs' endoskeletons showing a mineralized, tessellated layer that is sandwiched between a hyaline cartilage core and an outer fibrous, connective tissue called perichondrium.
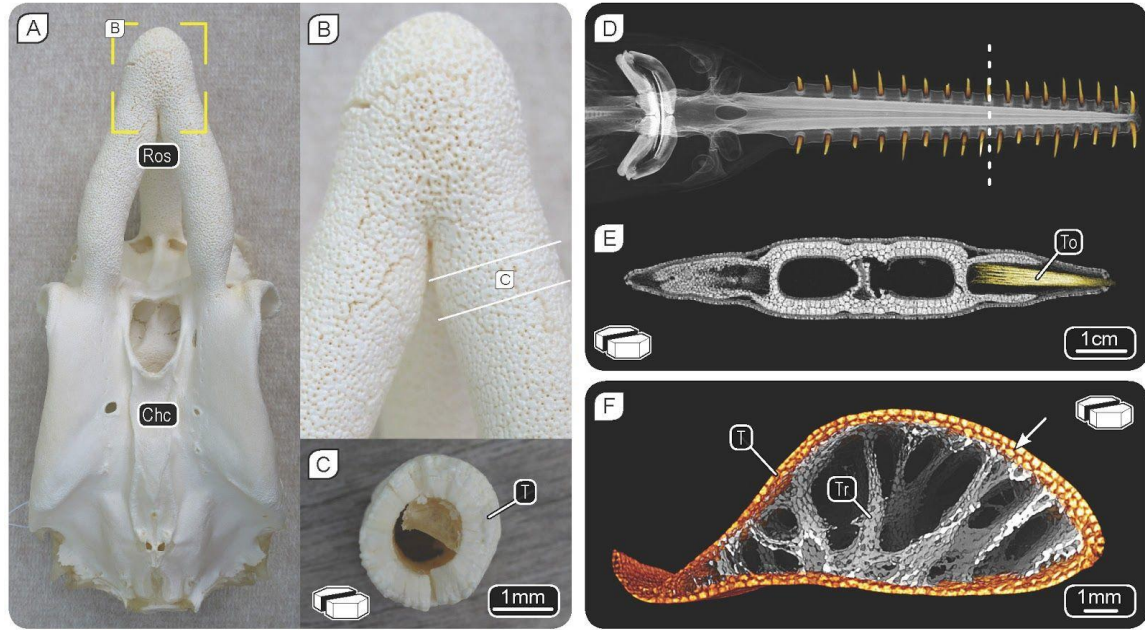
Figure 2. Modifications of tessellated calcified cartilage for skeletal reinforcement.
A-B) Chondrocranium (Cho) of a mackerel shark *Lamna nasus*, showing the thickened bars of the rostrum (Ros), characteristic of this genus. **C)** Cross section of the rostrum as indicated in B) showing multiple layers of large, "columnar" tesserae. **D)** Computed tomography image of the chondrocranium and rostrum/saw of the sawfish *Pristis microdon* **E)** showing 2-3 close-fitting/tight layers of tesserae and a tooth (To) in cross section of the saw. **F)** Computed tomography image of a cross section of the lower jaw of a cownose stingray *Rhinoptera bonasus*, exhibiting supernumerary tesseral layers (T; arrow) and trabeculae (Tr).

All of these mineralized tissues represent variations on the theme of tessellated calcified cartilage and suggest a role in reinforcing skeletal elements, even though they are not all found in areas likely to experience heavy loads. Here, we define a new form of calcified cartilage in elasmobranchs, which is associated with tessellated calcified cartilage, but apparently not derived from it. The skeletal features we describe here —which we refer to as endophytic masses (EPMs)— are a drastic departure from the previously described forms, and therefore suggest a new and entirely different process of cartilage calcification. Using a variety of materials and biological tissue characterization techniques, including histology, polarized light microscopy, electron microscopy and diffraction studies, we show that EPMs exhibit an entirely different composition and ultrastructure compared to tesserae. Also, as we demonstrate that EPMs occur in a variety of disparate but related species, we argue that they are natural features of tessellated calcified cartilage, discussing also their origin and role in shark and ray skeletons.

METHODS

Species examined & sample preparation

We discovered EPMs in samples which had been prepared for another study (Seidel et al., 2016), either frozen and fixed for examination in microCT or plastic-embedded and sectioned for light and electron microscopy. All characterization/visualization techniques in the current study (excluding microCT, which was performed on whole, ethanol-fixed samples) use the plastic-embedded sections described below, with some techniques (histology, TEM) requiring further sample preparation to remove embedding material.

In addition, to verify that EPMs were not an artifactual result of sample preparation (e.g. ethanol dehydration and/or fixation), a variety of control samples were prepared. Fresh (non-fixed) hyomandibular or shoulder girdle (propterygium) samples from several shark and batoid species were examined either as manual cross-sections in light microscopy or as intact skeletal pieces in microCT. Furthermore, propterygium samples from *Urobatis halleri* and *Leucoraja naevus* were incubated for 5 months in either water, dehydrating agent (EtOH series) or other fixative media (paraformaldehyde, PFA) and observed regularly for EPM growth.

Jaw, hyomandibular, or propterygium cartilages were excised from frozen adult elasmobranch specimens (skates/rays: *Amblyraja radiata*, *L. naevus*, *Raja montagui*, *U. halleri*; sharks: *Negaprion brevirostris*, *Scyliorhinus retifer*); excepting *U. halleri* with three specimens, we examined one specimen per species. Specimens were acquired from bycatch from research cruises at other institutions, except for *S. retifer*, which were lab-raised. Samples were embedded in plastic resin (polymethyl methacrylate, PMMA), cut in slices (300±100μm thick; Buehler IsoMet low speed saw) and mounted on a PMMA object slide using double-sided adhesive tape. Sections were wet polished with silicon carbide papers with descending grain sizes (Logitech PM5 Precision Lapping and Polishing Machine), then polished using a soft polishing plate and diamond spray (0.25 μm grain size). For more detailed discussion of sample preparation, see Seidel et al. (2016).

Microcomputed tomography (microCT)

Hyomandibulae from an age series of *U. halleri* (7.0, 11.0, 14.4 and 19.0 cm disc width: DW, i.e. the maximum lateral dimension of the animal) were dissected and transferred through an ascending alcohol series, then stored for several weeks until scanning in 75% EtOH. For scanning, samples were gripped in hand-cut polystyrene cradles and sealed in PVA vials partially filled with 75% EtOH (to create a humidified scanning environment, but not touching the samples) and scanned with a Skyscan 1172 desktop microCT scanner (Bruker microCT, Kontich, Belgium). Scans for all samples were

performed with voxel sizes of 4.89 μm, at 59 kV source voltage and 167 μA source current, over 360° of sample rotation.

Backscatter scanning electron microscopy (BSE) and energy dispersive X-ray spectroscopy (EDS)

BSE microscopy allows the imaging of either changes in tissue elemental density or composition as grayscale variation. Images were acquired of polished PMMA-embedded samples from *N. brevirostris*, *U. halleri*, *L. naevus*, and *R. montagui* jaw, hyomandibular, and propterygium cartilages in backscatter mode using a Field Emission-Environmental Scanning Electron Microscope (FE-ESEM, FEI Quanta 600F) in environmental mode (i.e. at low vacuum without sputtering) with acceleration voltage of 10-12.5 kV.

To determine the nature of the grayscale variation observed in BSE, we examined samples from *L. naevus* propterygium cartilages under EDS using a JEOL JSM 7500F scanning electron microscope equipped with two Oxford X-Max 150 Silicon drift detectors. Using EDS, we compared the elemental composition of tesserae and EPMs in the skate *L. naevus* with regards to elements relevant to mineral formation (calcium, magnesium, sodium, phosphorus and sulfur). All EDS spectra and elemental maps were acquired at 20 kV acceleration voltage and paired with images of the same regions of interest taken under the same conditions in backscatter mode or with a secondary electron detector. To perform a semi-quantitative analysis on the mineral phases, a hydroxyapatite standard of known composition was measured to standardize the EDS quantification routines for Ca, O and P. As few data exist for elasmobranch skeletal tissue mineral composition or crystallography, a human bone sample of known elemental composition was also examined to validate the standardization. The bone sample, from an adult woman's femur, was provided by the Department of Forensic Medicine of the Medical University of Vienna, in accordance with the ethics commission board of this institution (EK#: 1757/2013); the sample had been stained with Rhodamine6G for another study, but this has no effect on our elemental analysis. All samples were coated with a conductive layer of carbon, and so this element was excluded from the semi-quantitative analyses; the composition data we report therefore sum to 100% without C.

Transmission Electron Microscopy (TEM)

For TEM, PMMA-embedded hyomandibulae samples from a skate (*R. montagui*) were used. PMMA was removed with acetone overnight and subsequently the samples were embedded in EPON resin. Serial ultrathin sections (150 nm) were cut on a Reichert Ultracut S microtome (Leica Microsystem, Wetzlar, Germany) with an ultra-diamond knife, and mounted on dioxan-formvar coated slot-grids (#G2500C, Christine Gröpl,

Elektronenmikroskopie, Tulln, Austria). Although these sections had high native contrast due to their slice thickness and did not require staining with uranyl acetate (ph = 3.5) and lead citrate (pH = 8.0), we stained every third section (Leica Ultrostainer, Leica Microsystem, Wetzlar, Germany) to highlight delicate structures such as collagen fibers. The sections were examined with a Philips CM 120 transmission electron microscope at 80kV (FEI, Eindhoven, Netherlands) equipped with a MORADA digital camera (Olympus SIS, Münster, Germany). To compare crystallographic characteristics of tesserae and EPMs, we performed selected area electron diffraction (SAED) using a ZEISS EM 912 Ω transmission electron microscope working at 120 keV. The TEM images were used to measure EPM crystal dimensions, and assuming that, in the various images acquired, the crystals are axially randomly oriented we estimated the 3D size of the crystals taking the maximum and minimum sizes perpendicular to the particles' long axes.

Raman spectroscopy

Raman spectra of three EPMs, tesserae and uncalcified cartilage within embedded samples were acquired from an *L. naevus* jaw vertical section using a confocal Raman microscope (CRM200, WITec GmbH, Ulm, Germany) equipped with a P-500 piezo-scanner (Physik Instrumente, Karlsruhe, Germany) and a CCD-sensor (Princeton Instruments Inc., Trenton, NJ). A 785 nm laser (Toptica Photonics AG, Graefelfing, Germany) was used to generate Raman scattering while minimizing autofluorescence and the resulting spectra were investigated using WITec Project software (v. 2.10, WITec GmbH, Ulm, Germany). Brushite and calcium pyrophosphate dihydrate (CPPD) were synthesized for comparison with EPM spectra. Synthetic brushite was precipitated with K_2HPO_4 (Sigma), Na_2HPO_4 (ChemCruz), and $CaCl_2 \bullet 2H_2O$ (Roth), as described in Temizel et al. (2011). Synthetic CPPD triclinic was synthesized according to Brown et al. (1963).

Polarized light microscopy (PLM)

PLM was performed on polished samples (sections of ~150-300 μm thickness) of *N. brevirostris*, *U. halleri*, *L. naevus*, and *R. montagui* jaw, hyomandibular, and propterygium cartilages, showing tesserae in vertical section (cross-sections with perichondrium on one side of the tessera and uncalcified cartilage on the other; Fig. 1), using a Leica microscope DMRXA2, camera DFC480, and the imaging software LAS X. The orientation of collagen fibers could be discerned since birefringence varied with fiber angle, with a maximum birefringence signal seen at +/-45° relative to the position of the microscope's polarizer and analyzer. We used a lambda filter to render positive and negative orientations with color contrast to allow finer scale distinction of EPM collagen fiber orientation.

Histology

Von Kossa (VK) staining was performed on the PMMA-embedded cross-sections (300 – 380µm) of hyomandibula of *L. naevus*. VK is typically used as a stain for mineralized tissues: VK stains phosphate ions that are common to calcium phosphate deposits (e.g. in mineralized tissues), via the precipitation of phosphate with silver ions, forming yellow/brown silver phosphate. The VK stain therefore indicates the presence of phosphates in calcium phosphate-based mineralized tissues (Kossa, 1901; Puchtler & Meloan, 1978), not calcium, as claimed by some authors (e.g. Ashhurst, 2004; Dettmeyer, 2011; Romeis, 1968). The silver stain is further reduced to black under strong light, via the reduction of silver into silver phosphate by surrounding organic material (Meloan & Puchtler, 1985).

To allow stain penetration, PMMA was removed with acetone for 2 hours, then sections were hydrated in a descending series of ethanol (100%, 90% and 70%) and rinsed in distilled water. Floating sections were incubated in 5% silver nitrate placed under light (60 watt light bulb) for 1 hour at room temperature (Allerstorfer et al., 2010; Álvarez et al., 2005; Blumbach et al., 2008; Blumer et al., 2012). Subsequently, they were rinsed in distilled water, and unreacted silver was removed with 5% sodium thiosulfate incubation for 5 minutes. Sections were rinsed again, mounted on glass slides and either embedded in entellan (after dehydration in ethanol) or distilled water without counterstaining. The sections were examined with a Zeiss Axioplan 2 (Zeiss, Oberkochen, Germany) and photographed as color images, using a Zeiss AxioCam HR and AxioVision 4.1. software. To increase the contrast of the sections, the aperture of the light microscope was closed slightly.

RESULTS

Endophytic masses (EPMs) were almost transparent in thin skeletal sections (<250 µm) using transmittance light microscopy (Fig. 3A). However, in thicker sections (~350 µm), using reflectance light microscopy, EPMs stood out as opaque, white masses against the nearly transparent uncalcified cartilage core of skeletal elements and the surrounding outer layer of mineralized cartilage (tesserae) (Fig. 3B). EPMs were found in a variety of the cranial and shoulder girdle skeletal elements observed, and in multiple species: a shark (*N. brevirostris*), one stingray (*U. halleri*) and two skates (*L. naevus*, *R. montagui*). EPMs did not form in any of the control samples prepared from *U. halleri* or *L. naevus* propterygia or hyomandibulae, incubated for up to 5 months in either water, EtOH series or PFA.

EPMs were typically associated with the inner, chondral edge of the mineralized tesseral layer, appearing semi-circular in cross-section with a diameter of ~300-500 µm (Fig. 3A-B). Sometimes, EPMs were found deeper inside the cartilaginous skeletal element, a short distance from the tessellated layer, but with no apparent association, being typically slightly larger than tesserae-associated EPMs (~200-600 µm in diameter) and exhibiting a more circular shape (Fig. 3B). We will focus primarily on the description of tesserae-associated EPMs for the remainder of the results, referring to them simply as EPMs.

EPMs were irregularly distributed within skeletal elements, with some sections lacking EPMs entirely while others contained multiple (e.g. 16 in ~85 mm^2 of uncalcified cartilage in Fig. 3B). The distribution was also inconsistent when comparing different hyomandibulae: of the several paired hyomandibulae (14 skeletal elements) we microCT scanned from several ages of *U. halleri*, EPMs were observed in only three hyomandibulae, from two different sub-adult animals (11 & 12 cm disc width, male & female, respectively; Fig. 3C). In total, 24 EPMs were found among these three CT-scanned hyomandibulae, with the largest number of EPMs (13) found in the right hyomandibula of the 11 cm disc width male. Despite the large of EPMs in this sample, they only occupied a small portion of the hyomandibula (0.05% by volume).
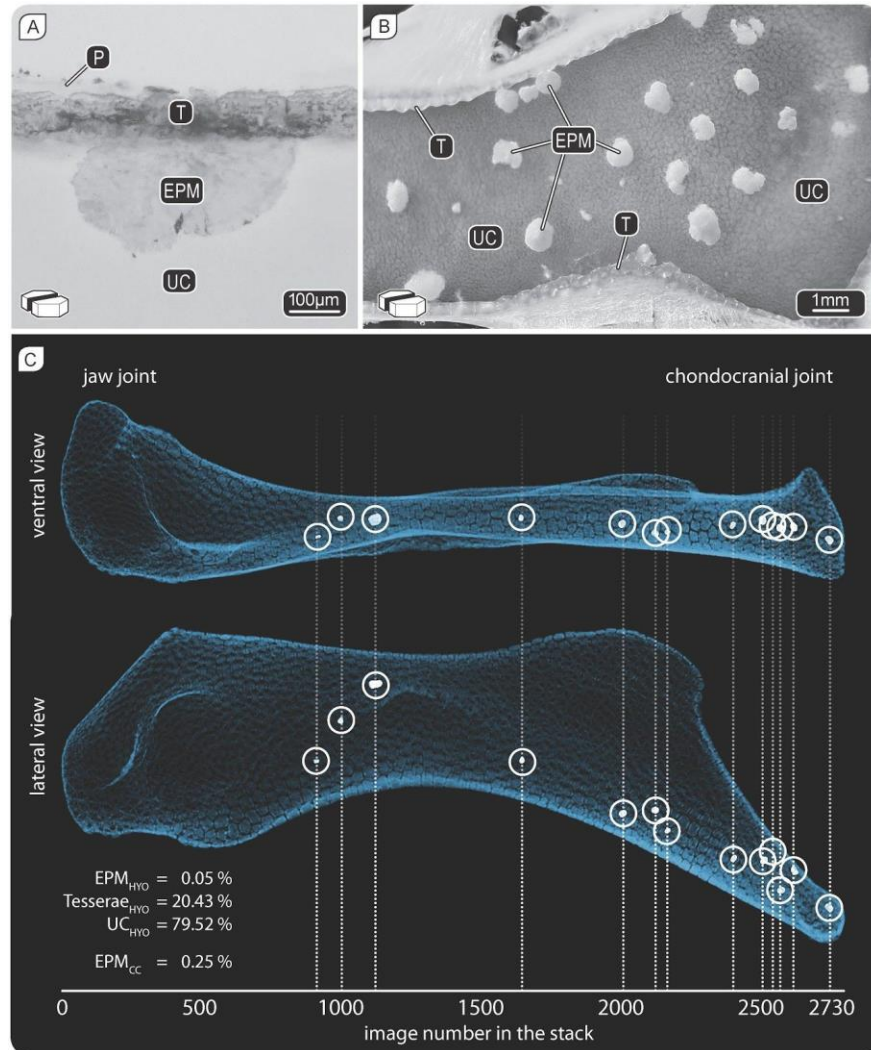
Figure 3. Distribution of endophytic masses (EPMs) in skeletal elements of elasmobranchs.
A) Transmittance light microscopy and **B**) reflectance light microscopy (LM) images of cross-sections of unstained skeletal elements (propterygia) from *N. brevirostris* and *L. naevus*, respectively, showing the tessellated cartilage layer in vertical view. In transmittance LM of thin sections (<250μm), EPMs and uncalcified cartilage (UC) appear almost transparent. Note in B) that some EPMs are associated with tesserae (T), while others are located deeper in the tissue (slice thickness: ~350μm). **C**) Micro-computed tomography imaging showing the occurrence of EPMs in the hyomandibula of *U. halleri*. EPMs constitute a very small volumetric percent of the overall skeletal element; volume fractions for each component of the skeletal tissue are listed on the lower left ($_{hyo}$= percentage of the total hyomandibula volume; $_{cc}$= percentage of the total calcified cartilage volume, tesserae and EPM).

EPMs occurred in particular at intertesseral joints or at intersections of several tesserae (Fig. 4). In many sections, individual EPMs exhibited narrow "stems" tethering them to the tesseral layer, squeezed between tesserae, so that EPMs appeared to protrude into the uncalcified cartilage like mushrooms (Fig. 4A, 5). The EPMs' mushroom-like bodies extended into the unmineralized cartilage on average a few hundred microns; however, their size varied considerably within skeletal elements. In

some sections, the EPMs' stems could be seen to extend through the tesseral mat up into the fibrous perichondrium layer, where the EPM matrix spread into the connective tissue in a relatively formless mass (Fig. 5A, C). The tissue surrounding EPMs (e.g. unmineralized cartilage, tesserae and perichondrium) appeared intact, without gaps or cracks, in most of the specimens. However, in some specimens the tesserae associated with the EPM were broken in little pieces (Fig. 5E), but we did not observe damage (no larger cracks, but micro-cracks may be present) of the unmineralized cartilage.
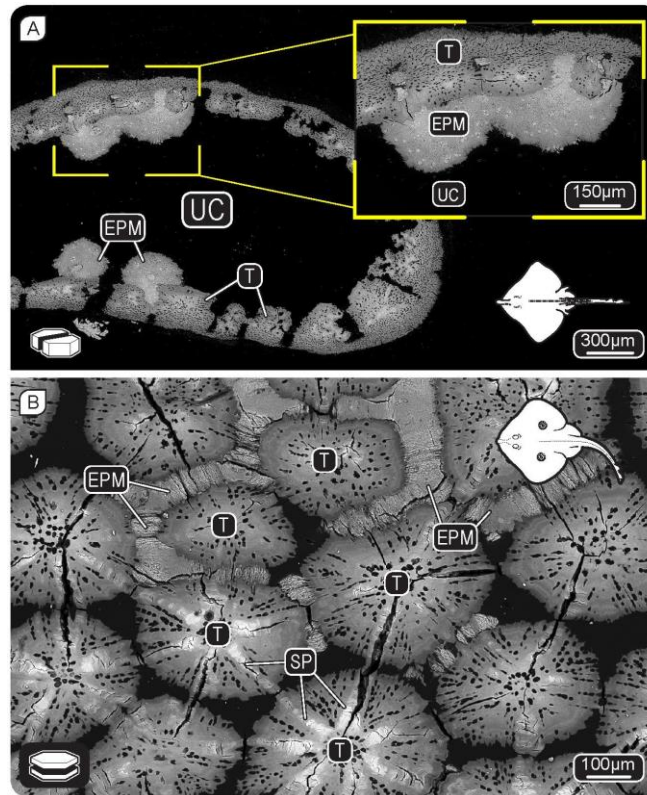

Figure 4. Mineralized, tesserae-associated endophytic masses
A) EPMs at intertesseral joints in vertical view (*R. montagui*) and **B**) at intersections of several tesserae in planar view (*L. naevus*). Mineralized EPMs appeared to cluster forming larger masses along the chondral edges of tesserae, covering larger areas and multiple intertesseral joints. In these backscatter SEM images, variation in grayscale represents mineral density variation, with the spokes (SP) within tesserae (T) showing the highest mineral density and the uncalcified cartilage (UC) the least. EPMs exhibit some variation in mineral density between specimens, but are typically comparable to the non-spoke regions of tesserae.

EPMs can be distinguished from surrounding tissues by several aspects of their structure and appearance. Both tesserae and EPMs are mineralized, evident from BSE images (Figs. 4 and 5) and VK staining (Figure 6), in contrast to the surrounding, non-mineralized musculature, connective tissue (i.e. perichondrium) and the uncalcified cartilaginous core of the skeleton (Fig. 4 and 5). The mineral density of the EPM matrix is relatively uniform across the tissue mass, but variable relative to tesserae, being at

times higher, lower or the same grayscale value (i.e. mineral density) as tesserae in the same BSE image (Fig. 5). The mineral density of the EPM matrix never appeared to exceed the highest mineral density features in tesserae, the hypermineralized "spokes" reinforcing intertesseral joints, visible in BSE (Fig. 4B and SG) (Seidel et al., 2016).
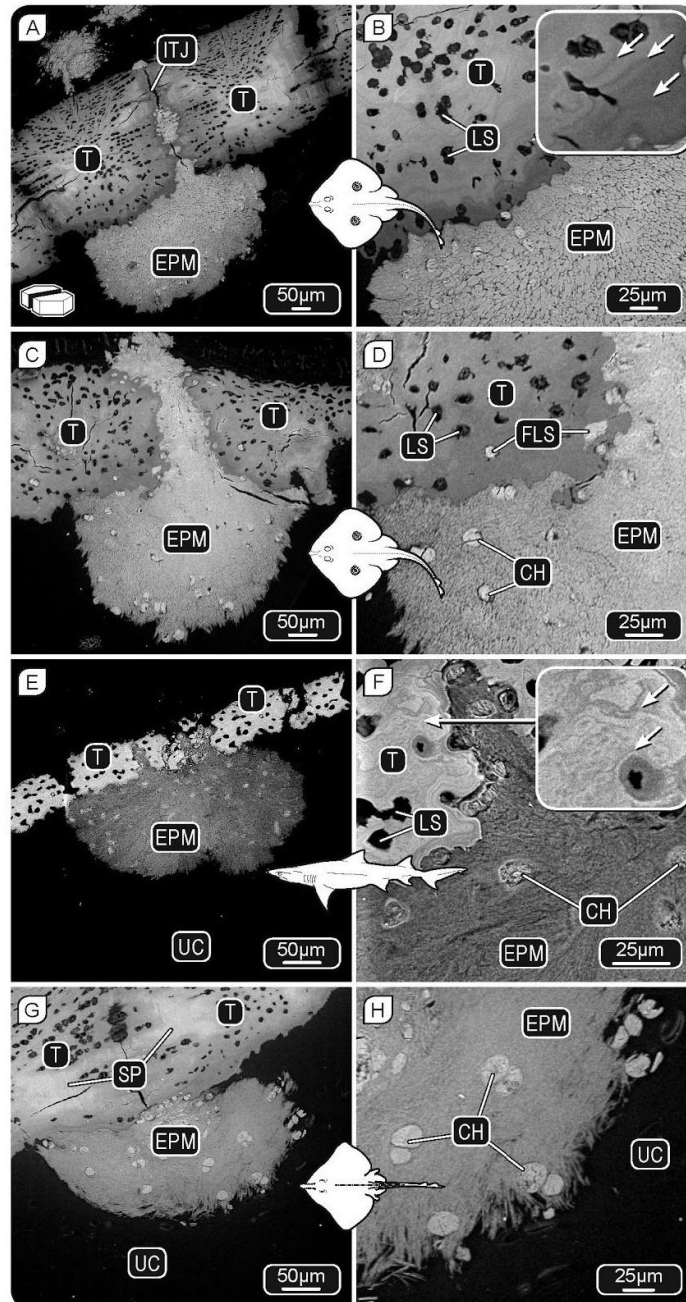

Figure 5. Ultrastructure of mineralized, tesserae-associated endophytic masses {EPMs)
Characteristic mushroom shape of individual mineralized EPMs associated with tesserae, in backscatter SEM images of vertical views from tessellated calcified cartilage of several elasmobranch species; A-D) *L. naevus;* E-F) *N. brevirostris;* G-H) *R. montagui.* EPMs occurred predominantly at intertesseral joints (ITJ), squeezing between two tesserae, growing into the unmineralized cartilage (UC). In some sections, EPMs appeared to

continue into the perichondrium on the "outer" side of the tesseral layer (image A, C). The tissue around EPMs appeared to be intact in almost all EPM sections. However, in some cases, tesserae were broken into several individual pieces, but no obvious damage of the unmineralized cartilage was observed (image E). The chondrocytes (CH) at the EPM mineralization fronts and within EPMs were dead and heavily mineralized. Also, the lacunar spaces (LS) in tesserae, which house alive chondrocytes, were sometimes filled with mineral (FLS) where they bordered EPMs (image D). Filled lacunar spaces exhibited a similar mineral density as the spokes (SP), the most pronounced features of adult tesserae (image G). Insets (image B, F) are magnifications showing Liesegang lines, another feature of mineral density in tesserae, which was not observed in EPMs.

EPMs contain cells of similar size (~10-15 µm long) and density to the living chondrocytes in the surrounding unmineralized cartilage and to the lacunar spaces (housing cells) in tesserae (i.e. Fig. 5). EPM cells, however, are uniformly dead and mineralized: note that, in contrast to the cells in the uncalcified cartilage and tesserae, EPM cells are visible in the BSE images in Fig. 5, due to their mineralization. The high mineral density of EPM cells is comparable to that of tesseral spokes (Seidel et al., 2016) and always exceeded that of the EPM body (e.g. Fig. 5). The cells within the lacunae of tesserae directly bordering the "stems" of the EPMs (i.e. flanking the intertesseral joints through which EPMs passed) were also often hypermineralized (Fig. 5C).
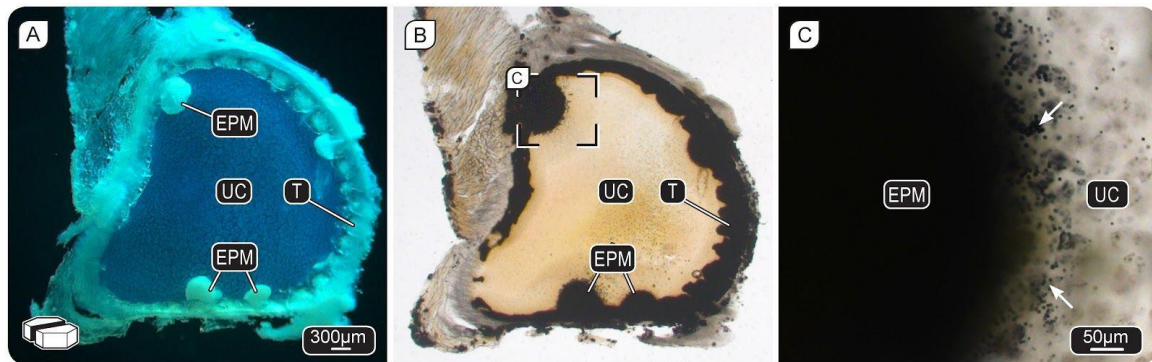

Figure 6. von Kossa staining of tesserae and EPMs.
A) Reflectance light microscopy images of opaque EPMs in the almost transparent uncalcified cartilage (UC) of unstained skeletal elements (propterygia) from *L. naevus* (slice thickness: ~ 350µm). **B**) The same section from A) stained with VK to illustrate that both tesserae and EPMs are phosphate-containing tissues; coupled with backscatter SEM data (e.g. Figs. 4-5), this verifies that both are calcified tissues. **C**) Small cell-associated granules in the unmineralized cartilage near the EPM mineralization front were visible (white arrows), in long-incubated VK-stained samples, but never short-incubated samples, nor in BSE, nor TEM imaging. The cells containing these granules (nearly invisible here due to lack of staining) are likely precursors to mineralized cells in EPMs and otherwise look similar to chondrocytes further away from the EPM.

The texture of the mineralized matrix in tesserae and EPMs is strikingly different. Whereas tesserae are characterized by a compact mineralized tissue with visible lines of

accretive growth (Liesegang lines; Fig. 5B,F; e.g. Kemp & Westrin, 1979 and Seidel et al., 2016), EPMs are visibly fibrous, exhibiting a brushstroke-like pattern of birefringent mineralized fibers, arranged in bundles that appear to be randomly oriented (Fig. 5 and 7). The mineralized fibers of the EPMs splay into the surrounding UC matrix, resulting in the EPM-UC interface often having a "frayed" appearance, in contrast with the defined, smooth chondral margins of tesserae (Fig. 4, 5).
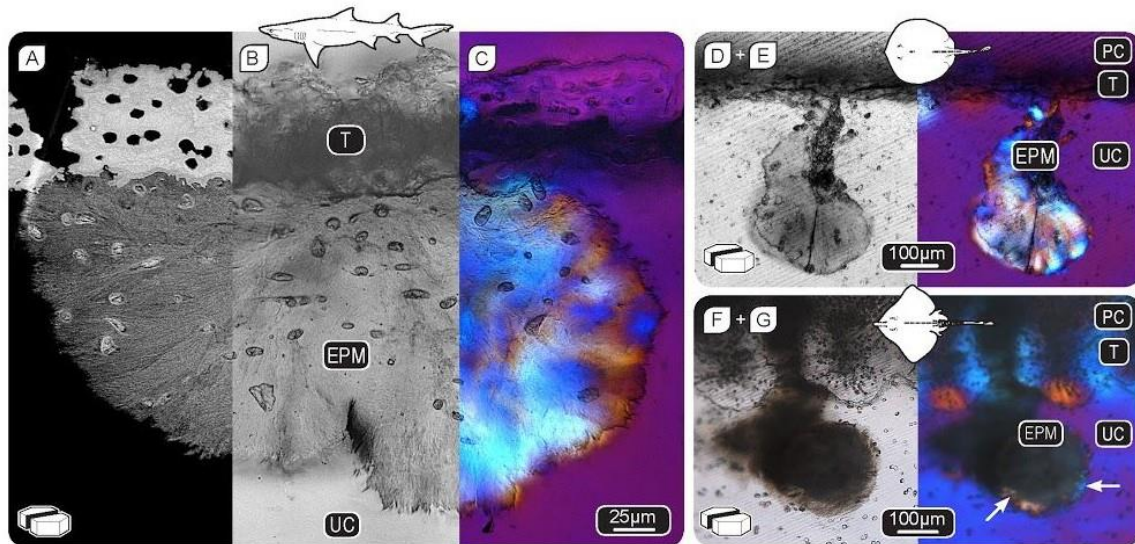

Figure 7. Birefringence and ultrastructure of EPMs.
A-C) Vertical section of a tessera-associated EPM in *N. brevirostris* in A) backscatter SEM imaging, B) transmitted light microscopy and C) polarized light microscopy with lambda filter showing EPMs' birefringent fibrous texture and frayed margins. **D-G**) Transmitted light and polarized light microscopy of tesserae-associated EPMs in vertical view of two different species, highlighting the variation in the degree of EPMs' birefringence which was not related to the slice thickness. D-E) EPMs in round stingray *U. halleri* were highly birefringent, whereas F-G) EPMs in *R. montagui* exhibited only little birefringence mostly at the margins (arrows), suggesting that the variation in birefringence can be either linked to developmental stages or ultrastructural differences.

Only in VK-stained samples, we observed arrays of black, ovoid granules (1 - 10 µm; Fig. 6A-B), haloing the "frayed" margin of EPMs. Granules were closely associated with UC chondrocytes, but it was unclear whether they were localized in or outside of cells (Fig. 6C). Granules were clustered into large masses directly along the EPM edges, with larger granules often appearing as conglomerations of at least two smaller granules, and with granules becoming smaller and more sparse with increasing distance from EPMs (Fig. 6C). Granules were not observed when a VK protocol with shorter incubation time (illuminated for less than 5 minutes) was used.
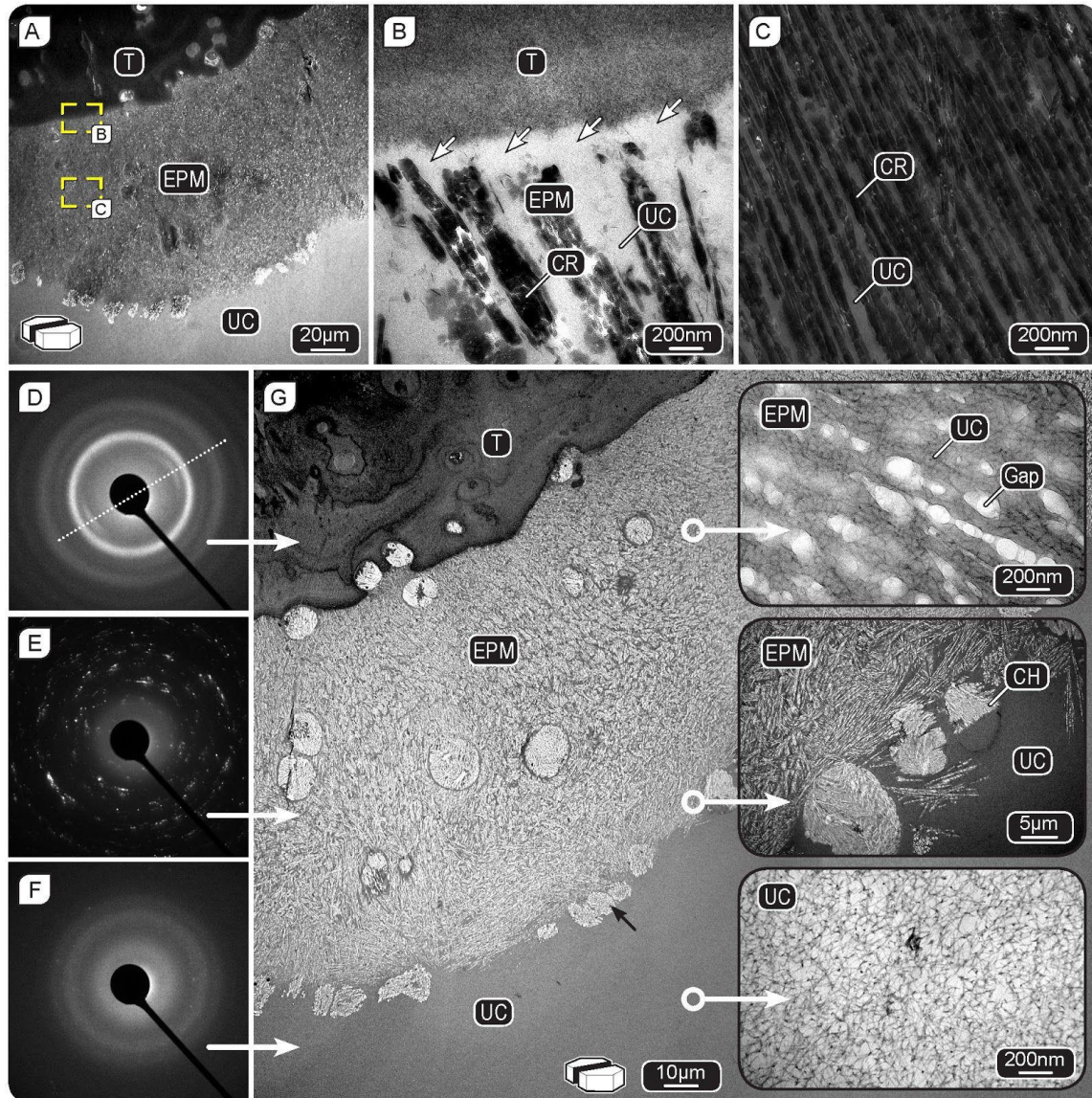
Figure 8: TEM micrographs and SAED patterns of elasmobranch skeletal cartilage.
A-C) Unstained thin-sections of tessera-associated EPMs of *R. montagui* showing the profound differences in crystal size and density between tesserae (T) and EPMs, with the latter exhibiting large, aligned crystals (Cr) forming long strings of crystals, embedded in unmineralized cartilage (UC). Tesserae and EPMs were commonly separated from one another by small gaps of unmineralized cartilage (white arrows in B). **D-F**) SAED patterns of D) a tessera, E) an EPM and F) unmineralized cartilage. Comparison of D) and E) illustrates the extreme difference in crystal size between tesserae and EPMs, while also showing that D) crystallites in the chondral margin of tesserae are aligned roughly parallel to the tesseral edge. **G**) Stained thin-section of a tessera-associated EPM showing type-2 collagen based uncalcified cartilage (UC) interspersed between EPM crystals. Gaps in the UC matrix represent former positions of crystals, which were removed in the staining process due to the acidic properties of uranyl acetate (see Material and Methods). Mineralized chondrocytes in the EPM and at the EPM edge (black arrow, and middle inset) show high crystal densities, suggesting a lower portion of organics in the cells compared to the extracellular matrix (UC).

The mineral phase of the EPM exhibits pronounced differences relative to that of tesserae, visible particularly in TEM micrographs (Figure 8). In unstained sections of EPMs (Fig. 8A-C), we observed large single, elongated platelets (estimated to be ~500x250x100 nm in size from TEM images), aligning end to end in long strings. These crystal strings are embedded in an organic matrix, which is similar in appearance and with a similar SAED pattern to the uncalcified cartilage (Fig. 8F,G). This is reflected in the corresponding SAED patterns, which are characterized by scattered, isolated and very sharp spots, indicating that this phase is composed of micron-scale single crystals (Fig. 8E). The radially integrated diffraction patterns cannot be unequivocally assigned to a specific calcium phosphate phase, but the large number of detected reflections and their small separation is compatible with low-symmetry CaP phases: brushite ($CaHPO_4 \cdot 2H_2O$) or monetite ($CaHPO_4$) or CPPD ($Ca_2P_2O_7 \cdot 2H_2O$) (Bjelle 1972; McCarty et al., 1966). Also, this phase appears to contain a higher amount of P and O than the tesseral mineral phase, and is depleted in Na and Mg, suggesting less substitution (Fig. 10). This observation is consistent with the single crystalline nature of the EPM mineral phase. Interestingly, the semi-quantitative compositional analysis of this phase reveals that it is characterized by a Ca/P ratio close to 1. This is compatible with brushite, monetite or CPPD, but the mineral phase of the EPM cannot be identified unambiguously by EDS alone.

Raman microspectroscopic data acquired on EPMs supported EDS and SAED findings (see below) that EPMs are comprised of a Ca and P-rich crystalline phases (Fig. 10B-C). A survey of Raman spectra collected from different EPMs showed two ν_1 phosphate peak shapes, either a broad peak (930-1020 cm^{-1}; EPM-1 in Fig. 19B-C) or a narrow peak (~960-1010 cm^{-1}; EPM-2 in Fig. 10B-C), both with peak position at ~985 cm^{-1}. The narrow peak closely resembled the ν_1 phosphate peak of brushite (Fig. 10B-C) (Casciani & Condrate, 1979; Penel et al., 1999). The shoulder of the broad ν_1 phosphate peak of EPM-1 could result from a convolution with a mineral phase similar to tesseral apatite (959 cm^{-1}). The primary peak of synthetic CPPD (1037 cm^{-1}) was not evident in EPM spectra.

Selected area electron diffraction (SAED) patterns obtained on tesserae showed several broad rings (see Fig. 8D), as typically observed for nanosized particles, and exhibited preferential orientation roughly parallel to the tessera's chondral edge. The position of the reflections in radially integrated patterns (not shown) is fully consistent with apatite, supporting findings from previous diffraction work on elasmobranch tesserae and vertebrae (Applegate 1967; Omelon et al., 2014; Urist, 1961, 1962). Furthermore, from the analysis of the angular dependence of the (002) apatite reflections, it can be inferred that the c crystallographic axis of the nanoparticles lies parallel to the collagen fibers, as found in other vertebrate hard tissues like bone (Ascenzi et al., 1979; Fratzl et al., 2004 and references within; Jaschouz et al., 2003) and

mineralized turkey tendon (Bigi et al., 1988). The Ca/P atomic (often referred to as molar) ratios measured by EDS for the tesseral apatite (Fig. 9) range between 1.2 and 1.3, much smaller than the theoretical value for apatites (1.67) and lower than those reported for elasmobranch vertebrae (1.52; Urist, 1961) and bone apatites, the values of which have been reported to range from 1.5 to 1.85, depending on the sample preparation and analysis techniques used (e.g. Bigi et al., 1997; Grynpas et al., 1991; Landis et al., 1978; Legros et al., 1987; Mahamid et al., 2011; Obrant & Odselius 1985; Ravaglioli et al., 1996) However, the high content of sodium (Na) and magnesium (Mg), which can substitute for calcium (Ca) in the apatite lattice, can explain this difference. It is worth noting from Na and Mg distributions that the degree of substitution varies spatially within tessera, and, in particular, increases from the center to the margin (Fig. 9).
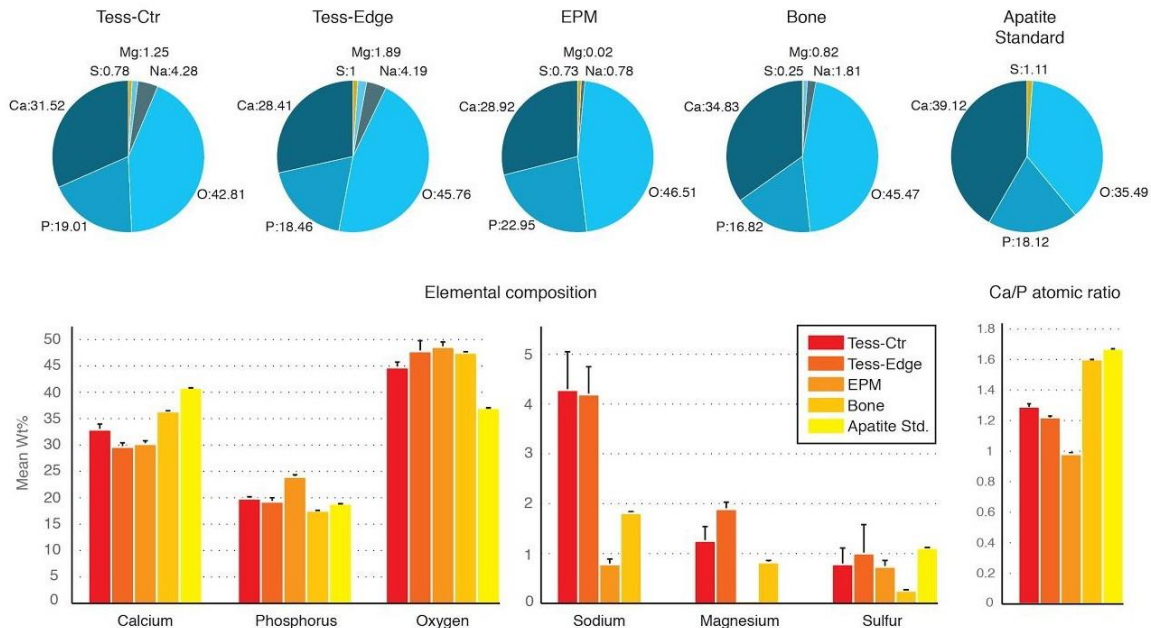

Figure 9. Chemical analysis of tesserae and EPMs in skate L. naevus.
Energy Dispersive Spectroscopy (EDS) data for two regions of tesserae (center and edge), EPM, and bone and apatite standards. All values are in mean wt%. Calcium to phosphorous atomic (often referred to as molar) ratios are provided in the lower right corner. Note, in particular, the differences between tesserae and bone/apatite samples and between EPM and tesserae. Abbreviation: Tess-Ctr = Tessera center, Tess-Edge = Tessera edge.
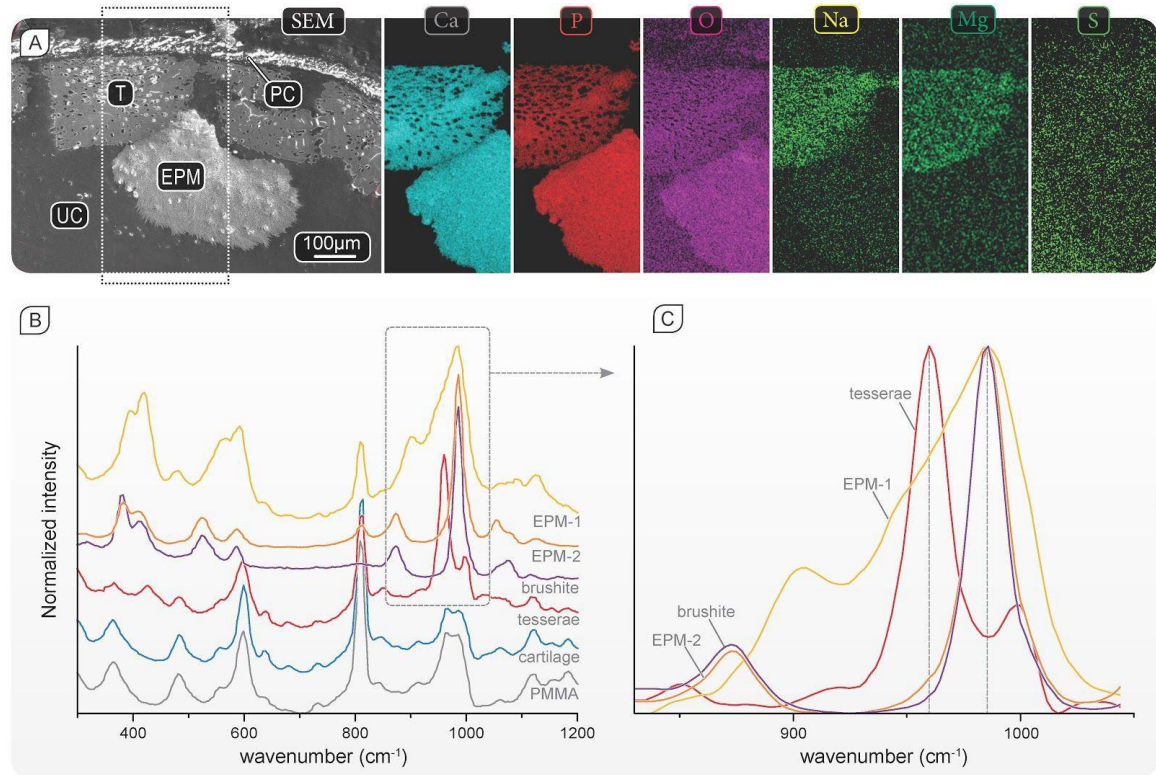
Figure 10. Elemental composition and Raman vibrational spectra of tessellated calcified cartilage and EPMs in skate L. naevus.

Backscatter SEM imaging and elemental maps of calcium (Ca), magnesium (Mg), sodium (Na), oxygen (O), phosphorus (P) and sulfur (S) concentrations in different elasmobranch tissues; perichondrium (PC), tesserae (T), unmineralized cartilage (UC) and a tesserae-associated EPM. B) Raman spectra of two different EPMs, tesserae, and uncalcified cartilage, as well as brushite and PMMA (embedding material) for comparison. C) Magnification of the $\nu 1$ spectral region of phosphates shown in the dashed gray box in (B); note the different position of the $\nu 1$ phosphate peak for EPM regions relative to tesserae and the similarity between the brushite spectrum and that of EPM-2.

DISCUSSION

Endophytic masses —a form of ectopic cartilage calcification we describe for the first time in elasmobranch fishes— were observed in a variety of skeletal elements and species, from both sharks and batoids (rays and relatives). Intra- and inter-species EPM comparisons revealed general anatomical commonalities in EPM shape, size, ultrastructure, association with intertesseral joints, and incorporation of high-mineral-density chondrocytes. Even though endophytic masses are closely associated with tesserae —the primary and ubiquitous mineralized component of the skeleton— bordering their chondral and lateral surfaces, their ultrastructure and crystallography differ significantly (Clement 1992, Kemp & Westrin 1979, Peignoux-Deville et al., 1982, Seidel et al., 2016). Tesserae bear record of an accretive and periodic growth process, in the form of agglomerations of mineralized sphericles ("calcospherites") at their chondral and lateral margins, and internal banding of varying mineral density (Liesegang lines; Fig. 5B and 8G; see also Ørvig, 1951; Dean et al., 2015; Seidel et al., 2016 and references within). In contrast, EPMs are comprised of long strings of plate-like crystals interspersed with scant volumes of a type-2 collagen-based matrix (Fig. 8G), similar to the surrounding uncalcified cartilage (Blumer et al., 2015; Enault et al., 2015). The organization of the crystals appears not to be linked to the collagen orientation in the cartilage. Although tesserae and EPMs are apparently both type-2 collagen-based tissues (Blumer et al., 2015; Enault et al., 2015), the differences in crystallite size and chemistry, and in the apparent mechanisms of tissue organization and mineral precipitation between them may explain why tesserae and EPMs were separated by unmineralized gaps and not fused (Fig. 8B). The striking mineralization pattern of EPMs and their non-ubiquity also argue that different mechanisms of skeletal cartilage mineralization underlie tesserae and EPM development.

EPM etiology

EPMs appear to be uncommon: we observed them in just three of the 14 hyomandibulae examined with microCT from several ages of round stingray *U. halleri*. The lack of mention of EPMs in previous literature is also conspicuous (but see Fig. 2 in Maisey, 2013, for what could be a non-tesserae-associated EPM in the jaw cartilage of the shark *Mustelus*). While the overall rarity of the EPMs raises the possibility that these features may be somehow produced by our sample preparation methods, as was recently reported with zinc oxide mineral precipitating in spider fang channels during dehydration (Politi et al., 2016), our experimental results suggest otherwise. Our control samples —incubated in either water, EtOH series or PFA— indicate that EPMs are not simply features resulting from dehydration or fixation. The presence of EPMs in intact, microCT-scanned hyomandibulae also argues that EPMs are not caused by cutting or trimming samples (e.g. by allowing materials from one tissue compartment

anomalous access to another). That EPMs are naturally occurring features in living animals and not artifacts is further supported by their apparent integration into (rather than displacement and rupture of) surrounding tissues, as well as the consistency of EPM size, shape and appearance in a variety of species.

That we did not observe EPMs in any fresh dissected samples implies that they may have a different appearance in non-fixed tissue (e.g. may be transparent) and that they may simply be uncommon. Our microCT-investigated age series of hyomandibulae suggests that EPMs would be found in 21.4% (=3/14) of samples from the same portion of the skeleton and in varying frequency when present. This is, however, even more prevalent than CPPD crystal deposition in human knee cartilage, which was observed in only 13% of elderly subjects in a large study of 608 cadaveric knees (Ryu et al., 2014). In that study, age, gender and degree of joint degeneration were strong predictors of CPPD deposition; additional work is necessary to determine whether EPM presence is correlated with similar factors.

The distinct texture of EPMs and their occurrence in regions that typically do not mineralize suggests that they could represent a failure of the processes that normally determine where mineralization occurs and where it is inhibited. Elasmobranch cartilage proteoglycans can inhibit mineral precipitation *in vitro* (Gelsleichter et al., 1995), and are broken down at skeletal mineralization fronts *in vivo* (via degradation and/or desulfonation of glycosaminoglycan chains; Takagi et al., 1984). Furthermore, matrix Gla protein (MGP), a binder of mineralization ions and inhibitor of soft tissue calcification (Luo et al. 1997), has been found adjacent to vertebral and tesseral mineralization fronts in blue sharks, *Prionace glauca* (Ortiz-Delgado et al., 2005). There is also growing indication that chondrocytes play a role in elasmobranch cartilage calcification by controlling their local environment via expression of mineralization inhibitors and promoters. Cells near tesserae appear to express the highest concentrations of MGP (inhibitor; Ortiz-Delgado et al., 2005), while also occupying regions of high concentration of polymers of phosphate (polyPs) and the enzyme alkaline phosphatase (ALP), which cleaves polyPs to increase local inorganic phosphorous ion concentration for mineralization (Omelon et al., 2014; Urist, 1962). Several authors have also described what are apparently cell-associated vesicles at the tesseral mineralization front (e.g. Bordat, 1988; Clement, 1992; Kemp & Westrin, 1979; Takagi et al., 1984), suggesting that cells may secrete a packaged, metastable mineral precursor into the extracellular matrix to be delivered to mineralizing areas and transformed into apatite.

These pieces of evidence imply that EPM formation could be favored under abnormal conditions that upset local tissue homeostasis. Ectopic mineralization could conceivably be triggered by a decrease in local proteoglycan content that allows mineralizing ions more access to collagen fibers (as proposed for some mammalian cartilage diseases; Gallagher et al., 2015; Kalya & Rosenthal, 2005; Kemp & Westrin,

1979), a change in chondrocyte health, or a decrease in pH below the neutral pH of elasmobranch body sera (see citations in Supplementary Table 4: Dean et al., 2015) since the calcium phosphate mineral suggested by our data (brushite) precipitates in acidic solutions (pH ~5; Galea et al., 2013; Shellis et al., 1997).

The argument that EPMs represent a disruption to local homeostasis is supported in particular by EPM-associated cells, which are "micropetrotic" (filled by hypermineralized material). Our data suggest that cells do not die from being encapsulated in mineralized EPM tissue (as with micropetrotic cells in bone; Carpentier et al., 2012; Frost, 1960; Remaggi et al., 1996). Rather it appears that cells need only come into contact or proximity with EPMs to become mineralized (Fig. 5H and 8G). EPM micropetrosis is also apparently not a function of animal age, in contrast to the micropetrosis described recently for intratesseral chondrocytes in *U. halleri* (Seidel et al., 2016). Whereas mammalian cartilage and bone cells are known to die as a function of tissue damage (Cardoso et al., 2009; Martin et al., 2015; Verborgt et al., 2000), we saw no evidence of *in vivo* damage (e.g. clefts) in EPM-associated tesserae or unmineralized cartilage. Furthermore, the shape and size of partially-mineralized cells external but near to EPMs appeared otherwise similar to unaffected cells further away in the unmineralized cartilage core.

EPM-adjacent cells, however —and not cells neighboring active tesseral mineralization fronts (i.e. chondral and intertesseral margins)— were the only ones associated with the von Kossa-positive granules that we observed during long (but not short) staining incubation times (Fig. 6). The granules were not detectable in backscatter SEM (i.e. they were not mineralized) or in EDS, but were of similar sizes and shapes to the cell-associated vesicles previously hypothesized to be involved in elasmobranch cartilage mineralization (Clement, 1992; Kemp & Westrin, 1979; Takagi et al., 1984). The delayed VK staining we observed could be due to sample preparation resulting in inorganic phosphates being freed from an unknown endogenous phospho-complex (e.g. via polyP degradation; Omelon et al., 2014). Even if granule staining is somehow artifactual (e.g. the result of the stain associating with organic material; see Puchtler & Meloan, 1978, 1985 and references within), their consistent placement within or in the vicinity of EPM-adjacent cells and their condensed morphologies indicate that elasmobranch chondrocytes and their pericellular environments undergo distinct changes in association with the development of EPMs.

EPMs in context

Although EPMs have not been previously documented, they resemble other ectopic tissues reported in elasmobranch fishes. Studies have noted mineralized fusions of tesserae (Applegate, 1967; Maisey, 2013), in some cases taking the form of massive "hypercalcified" masses on the perichondral side of the tesseral layer (Fig. 10 in Maisey,

2013), resulting in a stiff covering to the skeleton. It is not clear whether the "hypercalcified" masses also continued onto the chondral side of the tesseral layer. EPMs could represent an earlier stage in the formation of the massive hypercalcifications/fusions described by Maisey (2013). Many authors have also observed pathologic, mineralized masses encasing portions of the vertebral column in sharks (Hoenig & Walsh, 1983; Huber et al., 2013; Officer et al., 1995; Porter et al., 2006), particularly in captive sandtiger sharks (*Carcharias taurus*) with spinal deformities (Fig. 11A), encasing sites of former vertebral fracture or dislocation (Fig. 11B-C) (Huber et al., 2013). This excessive mineralization occurs within the fracture gaps of damaged individual vertebrae (endophytic mineralization), but also outside the margin of the notochordal sheath (exophytic mineralization), with the latter being the source of mineral overgrowth that results in fusion of adjacent vertebrae.

Previous studies of elasmobranch "hypercalcified" masses and vertebral calluses did not characterize ultrastructure or mineral phase and so cannot be compared with our data. However, a commonality of EPMs, "hypercalcified" masses and vertebral calluses is that they all involve the fusion of mineralized portions of skeletal elements. The cause of "hypercalcified" masses is unclear. The descriptions of vertebral calluses, however, suggest that they are specific responses to vertebral column damage (e.g. subluxation), perhaps triggered by local injury to the notochordal sheath (Huber et al., 2013). Similarly, but on a smaller scale, EPMs could be a response to damage, either to tesserae, the surrounding soft tissues (i.e. the unmineralized cartilage and perichondrium) or to the cells occupying the narrow gaps between tesserae, forming a mineralized and heterogeneous matrix to span and stabilize fracture gaps to facilitate repair, as in bone calluses (Fratzl & Weinkamer, 2007; Hoerth et al., 2014). In this way, ectopic mineralization could actually serve an adaptive function, stabilizing lesions and containing the spread of damage or infection, as has been suggested for inflammation-associated, pathological calcification in mouse and human vasculature (Abdelbaky et al., 2013; Abedin et al., 2004; Aikawa et al., 2007). To date, however, evidence suggests that elasmobranch skeletons cannot resorb or remodel tesserae in response to damage (e.g. *in vivo* experimental fracture of skeletal elements; Ashhurst, 2004; Clement, 1986), and that those calluses that do form in damaged tessellated tissue are fibrous, not mineralized (Ashhurst, 2004).
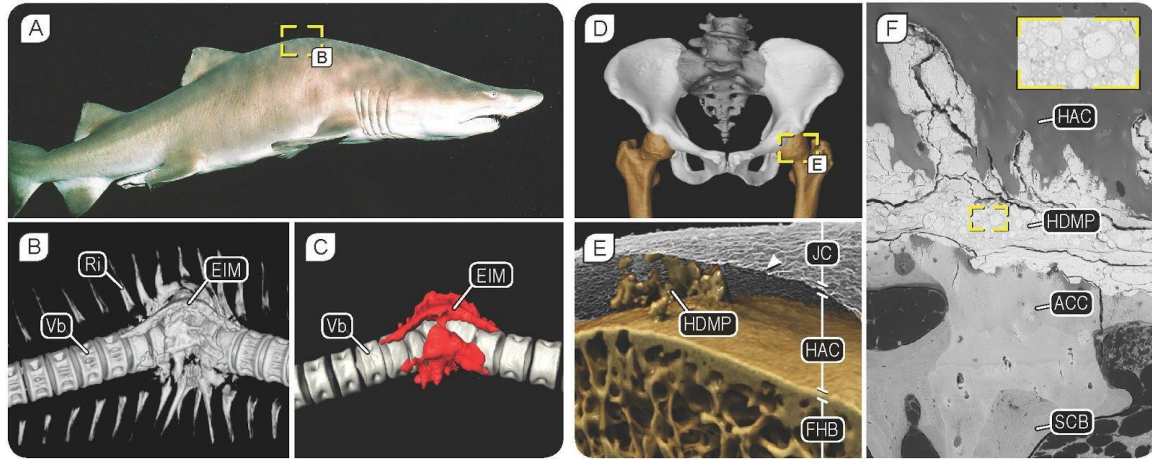
Figure 11. Skeletal pathologies in vertebrates (cartilaginous fish and human)
A) Photograph of a captive sandtiger shark (*Carcharias taurus*, Elasmobranchii) with spinal deformity (yellow frame). **B-C**) Computed tomography imaging of spinal deformation from *C. taurus,* with exophytic idiopathic mineralization (EIM) associated with vertebrae (Vb) and ribs (Ri). **D**) CT scan of a human pelvis with lumbar vertebrae and femora, indicating the location of joint shown in image E (yellow frame) **E)** Micro-computed tomography image of hyperdense mineralized protrusions (HDMP) protruding into the hyaline articular cartilage HAC covering a femoral head (FHB) with advanced osteoarthritis. The HAC has been rendered transparent to visualise HDMPs, and the arrowhead indicates the surface of the HAC within the joint capsule (JC). **F)** Backscatter SEM image showing the different mineral densities of subchondral bone (SCB), articular calcified cartilage (ACC) and HDMPs, and the globular ultrastructure of the latter.

From an anatomical perspective, EPMs are perhaps more similar to mammalian joint destructive pathologies, such as chondrocalcinosis (e.g. pseudogout) and high density mineralized protrusions (HDMPs). Chondrocalcinosis describes the deposition of calcium salts —brushite, calcium pyrophosphate (CPP), and/or basic calcium phosphate (BCP)— within joint articular cartilage or fibrocartilage and is often associated with the development and progression of osteoarthritis (Kalya & Rosenthal, 2005; McCarty et al., 1966). In chondrocalcinotic cartilage, as with elasmobranch EPMs, poorly formed, mineralized masses form within the extracellular matrix and are visible using radiographic techniques (Barskova et al., 2013; McCarty et al., 1966). Although we do observe evidence of brushite (and possibly other CaP minerals) in EPMs, we could not conclude that matrix proteoglycans or calcium-binding proteins have been altered in EPM production, as would be the case in chondrocalcinosis (Kalya & Rosenthal, 2005). Yet, the lack of chondrocyte hypertrophy and of visible damage to the matrix and fibers surrounding cells —hallmarks of chondrocalcinosis— illustrate the etiologies of EPMs and chondrocalcinotic cartilage differ at fundamental levels.

HDMPs, described recently in human and racehorse joint cartilage, are abnormal mineralized protrusions of the calcified cartilage layer surmounting the bone, jutting into the superficial unmineralized hyaline cartilage (Fig. 11C-D) (Boyde et al., 2011, 2014). It appears that HDMPs form in the cracks in the subchondral plate that follow

abnormal cartilage matrix stiffening, which can be caused by age- or disease-related modifications of the proteoglycans that typically protect collagens and inhibit mineralization of cartilage (Gallagher et al., 2015). Like EPMs, HDMPs exhibit comparatively high mineral density and grow endophytically into uncalcified cartilage. However, their presence in clearly damaged areas and their structure —lacking cells and comprised of dense globular mineral accretions rather than large, individual crystals— argue that their similarity with EPMs ends there.

CONCLUSIONS

EPMs are a distinct and comparatively rare mineralized tissue in elasmobranch skeletons, that differ considerably from tesserae in their ultrastructure and chemistry. Although the presence of EPMs in multiple species argues for their being a natural part of elasmobranch skeletal biology, their apparent inconsistency of location (i.e. not only in high-load areas) and the lack of coexisting tissue damage suggests they are a result of conditions that are not universal.

We conclude that a local breakdown of CaP mineralization inhibition processes is a likely cause for EPM formation. The micropetrotic cells within and bordering EPMs and the observation of von Kossa-positive granules haloing EPM-adjacent chondrocytes suggest that changes in local tissue homeostasis may precede EPM formation, as has been shown for some joint destruction diseases in mammals. Although there was no visible damage or degradation of the unmineralized cartilage surrounding EPMs, EPM ultrastructure and crystallography suggest multiple similarities with mineral deposition disorders in elasmobranch but also mammalian cartilage (e.g. chondrocalcinosis associated with osteoarthritis and HDMPs). Elasmobranch cartilage could therefore prove a useful and novel comparative model for joint destructive diseases and osteoarthritic micropetrosis.

Characterization of EPM development and surrounding matrix properties will be vital to developing elasmobranch cartilage as a model, perhaps in skates (Rajidae), where EPMs appear to be quite common and particularly prominent when present (e.g. Fig. 3). Further studies could focus in particular on biochemical changes that characterize the transition from unmineralized to mineralized cartilage in elasmobranchs, in the case of controlled apatite formation in tesserae, and the mineralization products described in this work. Parameters to investigate include changes in proteoglycan and polyP content, pH, and ALP activity at both EPM and tesserae mineralization fronts.

ACKNOWLEDGEMENTS

REFERENCES

Abdelbaky, A., Corsini, E., Figueroa, A.L., Fontanez, S., Subramanian, S., Ferencik, M., Brady, T.J., Hoffmann, U., Tawakol, A., 2013. Focal arterial inflammation precedes subsequent calcification in the same location: a longitudinal FDG-PET/CT study. Circ Cardiovasc Imaging 6, 747–754.

Abedin, M., Tintut, Y., Demer, L.L., 2004. Vascular calcification. Arteriosclerosis, thrombosis, and vascular biology. 24, 1161-1170.

Aikawa, E., Nahrendorf, M., Sosnovik, D., Lok, V.M., Jaffer, F.A., Aikawa, M., Weissleder, R., 2007. Multimodality molecular imaging identifies proteolytic and osteogenic activities in early aortic valve disease. Circulation 115, 377–386.

Allerstorfer, D., Longato, S., Schwarzer, C., Fischer-Colbrie, R., Hayman, A.R., Blumer, M.J.F., 2010. VEGF and its role in the early development of the long bone epiphysis. Journal of anatomy 216, 611–624.

Applegate, S.P., 1967. A survey of shark hard parts, in: Gilbert, P., Mathewson, R., Rall, D. (Eds.). Johns Hopkins University Press, Baltimore, Maryland, pp. 37–66.

Ascenzi, A., Bonucci, E., Generali, P., Ripamonti, A., Roveri, N., 1979. Orientation of apatite in single osteon samples as studied by pole figures. Calcif Tissue Int 29, 101–105.

Ashhurst, D.E., 2004. The cartilaginous skeleton of an elasmobranch fish does not heal. Matrix Biology 23, 15–22.

Álvarez, J., Costales, L., Serra, R., Balbín, M., López, J.M., 2005. Expression Patterns of Matrix Metalloproteinases and Vascular Endothelial Growth Factor During Epiphyseal Ossification. Journal of Bone and Mineral Research 20, 1011–1021.

Barskova, V.G., Kudaeva, F.M., Bozhieva, L.A., Smirnov, A.V., Volkov, A.V., Nasonov, E.L., 2013. Comparison of three imaging techniques in diagnosis of chondrocalcinosis of the knees in calcium pyrophosphate deposition disease. Rheumatology (Oxford) 52, 1090–1094.

Bigi, A., Cojazzi, G., Panzavolta, S., Ripamonti, A., Roveri, N., Romanello, M., Suarez, K.N., Moro, L., 1997. Chemical and structural characterization of the mineral phase from cortical and trabecular bone. J. Inorg. Biochem. 68, 45–51.

Bigi, A., Ripamonti, A., Koch, M., Roveri, N., 1988. Calcified Turkey Leg Tendon as Structural Model for Bone Mineralization. International Journal of Biological Macromolecules 10, 282–286.

Bjelle, A.O., 1972. Morphological Study of Articular-Cartilage in Pyrophosphate Arthropathy - (Chondrocalcinosis Articularis or Calcium Pyrophosphate Dihydrate Crystal Deposition Disease). Ann. Rheum. Dis. 31, 449–456.

Blumbach, K., Niehoff, A., Paulsson, M., Zaucke, F., 2008. Ablation of collagen IX and COMP disrupts epiphyseal cartilage architecture. Matrix Biology 27, 306–318.

Blumer, M., Seidel, R., Pechriggl, E.-J., Lyons, K., Dean, M., 2015. Cartilage or Bone? Collagens in "Cartilaginous" Fish Skeletons Answer an Old Question. Faseb Journal 29.

Blumer, M.J.F., Hausott, B., Schwarzer, C., Hayman, A.R., Stempel, J., Fritsch, H., 2012. Role of tartrate-resistant acid phosphatase (TRAP) in long bone development. Mech. Dev. 129, 162–176.

Bordat, C., 1988. Les cartilages calcifiés de la petite roussette (*Scyliorhinus canicula* L., Chondrichthyens): Histologie et ultrastructure. Canadian journal of zoology 66, 1432–1445.

Boyde, A., Davis, G.R., Mills, D., Zikmund, T., Cox, T.M., Adams, V.L., Niker, A., Wilson, P.J., Dillon, J.P., Ranganath, L.R., Jeffery, N., Jarvis, J.C., Gallagher, J.A., 2014. On fragmenting, densely mineralised acellular protrusions into articular cartilage and their possible role in osteoarthritis. Journal of anatomy 225, 436–446.

Boyde, A., Riggs, C.M., Bushby, A.J., McDermott, B., Pinchbeck, G.L., Clegg, P.D., 2011. Cartilage Damage Involving Extrusion of Mineralisable Matrix From the Articular Calcified Cartilage and Subchondral Bone. Eur Cell Mater 21, 470–478.

Brown, E.H., Lehr, J.R., Smith, J.P., Frazier, A.W., 1963. Preparation and Characterization of Some Calcium Pyrophosphates. Journal of Agricultural and Food Chemistry 11, 214-222.

Cardoso, L., Herman, B.C., Verborgt, O., Laudier, D., Majeska, R.J., Schaffler, M.B., 2009. Osteocyte Apoptosis Controls Activation of Intracortical Resorption in Response to Bone Fatigue. J. Bone Miner. Res. 24, 597–605.

Carpentier, V.T., Wong, J., Yeap, Y., Gan, C., Sutton-Smith, P., Badiei, A., Fazzalari, N.L., Kuliwaba, J.S., 2012. Increased proportion of hypermineralized osteocyte lacunae in osteoporotic and osteoarthritic human trabecular bone: implications for bone remodeling. Bone 50, 688–694.

Casciani, F., & Condrate Sr., R.A., 1979. The Vibrational Spectra of Brushite, $CaHPO_4 \cdot 2H_2O$. Spectroscopy Letters, 12, 699-713.

Clement, J.G., 1992. Re-examination of the fine structure of endoskeletal mineralization in Chondrichthyans: Implications for growth, ageing and calcium Homeostasis. Marine and Freshwater Research 43, 157–181.

Clement, J.G., 1986. Clement, J.G., 1986. Development, structure and composition of chondrichthyan skeletal tissues. Doctoral dissertation, PhD Thesis. London: University of London.

Compagno, L.J., 1988. Sharks of the order Carcharhiniformes, in: Princeton University Press Princeton, New Jersey.

Dean, M., Mull, C.G., Gorb, S.N., Summers, A.P., 2009. Ontogeny of the tessellated skeleton: insight from the skeletal growth of the round stingray *Urobatis halleri*. Journal of anatomy 215, 227–239.

Dean, M.N., 2011. Cartilaginous Fish Skeletal Tissues, in: Farrell, A.P. (Ed.), Encyclopedia of Fish Physiology. Academic Press, San Diego, pp. 428–433.

Dean, M.N., Ekstrom, L., Monsonego-Ornan, E., Ballantyne, J., Witten, P.E., Riley, C., Habraken, W., Omelon, S., 2015. Mineral homeostasis and regulation of mineralization processes in the skeletons of sharks, rays and relatives (Elasmobranchii). Seminars in Cell and Developmental Biology 46, 51–67.

Dean, M.N., Socha, J.J., Hall, B.K., Summers, A.P., 2010. Canaliculi in the tessellated skeleton of cartilaginous fishes. Journal of Applied Ichthyology 26, 263–267.

Dean, M.N., Summers, A.P., 2006. Mineralized cartilage in the skeleton of chondrichthyan fishes. Zoology 109, 164–168.

Dettmeyer, R., 2011. Forensic histopathology: fundamentals and perspectives. Springer Science & Business Media.

Dingerkus, G., Séret, B., Guilbert, E., 1991. Multiple prismatic calcium phosphate layers in the jaws of present-day sharks (Chondrichthyes; Selachii). Experientia 47, 38–40.

Enault, S., Muñoz, D.N., Silva, W.T.A.F., Borday-Birraux, V., Bonade, M., Oulion, S., Ventéo, S., Marcellini, S., Debiais-Thibaud, M., 2015. Molecular footprinting of skeletal tissues in the catshark *Scyliorhinus canicula* and the clawed frog *Xenopus tropicalis* identifies conserved and derived features of vertebrate calcification. Front. Genet. 6, 3133.

Fratzl, P., Gupta, H.S., Paschalis, E.P., Roschger, P., 2004. Structure and mechanical quality of the collagen– mineral nano-composite in bone. Journal of Materials Chemistry 14, 2115–2123.

Fratzl, P., Kolednik, O., Fischer, F.D., Dean, M.N., 2016. The mechanics of tessellations - bioinspired strategies for fracture resistance. Chem. Soc. Rev. 45, 252–267.

Fratzl, P., Weinkamer, R., 2007. Hierarchical Structure and Repair of Bone: Deformation, Remodelling, Healing, in: Self Healing Materials, Springer Series in Materials Science. Springer Netherlands, Dordrecht, pp. 323–335.

Frost, H.M., 1960. Micropetrosis. J Bone Joint Surg Am 42-A, 144–150.

Galea, L., Bohner, M., Thuering, J., Doebelin, N., Aneziris, C.G., Graule, T., 2013. Control of the size, shape and composition of highly uniform, non-agglomerated, sub-micrometer beta-tricalcium phosphate and dicalcium phosphate platelets. Biomaterials 34, 6388–6401.

Gallagher, J.A., Ranganath, L.R., Boyde, A., 2015. Lessons from rare diseases of cartilage and bone. Curr Opin Pharmacol 22, 107–114.

Gelsleichter, J.J., Musick, J.A., van Veld, P., van Veld, P., 1995. Proteoglycans from the vertebral cartilage of the clearnose skate, *Raja eglanteria*: Inhibition of hydroxyapatite formation. Fish Physiology and Biochemistry 14, 247–251.

Grynpas, M.D., Alpert, B., Katz, I., Lieberman, I., Pritzker, K., 1991. Subchondral Bone in Osteoarthritis. Calcif Tissue Int 49, 20–26.

Hoenig, J.M., Walsh, A.H., 1983. Skeletal lesions and deformities in large sharks. J. Wildl. Dis. 19, 27–33.

Hoerth, R.M., Seidt, B.M., Shah, M., Schwarz, C., Willie, B.M., Duda, G.N., Fratzl, P., Wagermaier, W., 2014. Mechanical and structural properties of bone in non-critical and critical healing in rat. Acta Biomaterialia 10, 4009–4019.

Huber, D.R., Neveu, D.E., Stinson, C.M., Anderson, P.A., Berzins, I.K., 2013. Mechanical properties of sand tiger shark (*Carcharias taurus*) vertebrae in relation to spinal deformity. Journal of Experimental Biology 216, 4256–4263.

Jaschouz, D., Paris, O., Roschger, P., Hwang, H.S., Fratzl, P., 2003. Pole figure analysis of mineral nanoparticle orientation in individual trabecula of human vertebral bone. Journal of Applied Crystallography 36, 494–498.

Kalya, S., Rosenthal, A.K., 2005. Extracellular matrix changes regulate calcium crystal formation in articular cartilage. Curr Opin Rheumatol 17, 325–329.

Kemp, N.E., S, Westrin, S.K., 1979. Ultrastructure of calcified cartilage in the endoskeletal tesserae of sharks. Journal of Morphology 160, 75–101.

Kóssa, G., 1901. Ueber die im Organismus künstlich erzeugbaren Verkalkungen. Beiträge zur pathologischen Anatomie und zur allgemeinen Pathologie;1901. Zweites Heft.

Landis, W.J., Glimcher, M.J., 1978. Electron diffraction and electron probe microanalysis of the mineral phase of bone tissue prepared by anhydrous techniques. J. Ultrastruct. Res. 63, 188–223.

Legros, R., Balmain, N., Bonel, G., 1987. Age-Related-Changes in Mineral of Rat and Bovine Cortical Bone. Calcif Tissue Int 41, 137–144.

Liu, X., Dean, M.N., Summers, A.P., Earthman, J.C., 2010. Composite model of the shark's skeleton in bending: A novel architecture for biomimetic design of functional compression bias. Materials Science and Engineering: C 30, 1077.

Liu, X., Dean, M.N., Youssefpour, H., Summers, A.P., Earthman, J.C., 2014. Stress relaxation behavior of tessellated cartilage from the jaws of blue sharks. Journal of the mechanical behavior of biomedical materials 29, 68–80.

Long, J.A., Burrow, C.J., Ginter, M., Maisey, J.G., Trinajstic, K.M., Coates, M.I., Young, G.C., Senden, T.J., 2015. First Shark from the Late Devonian (Frasnian) Gogo Formation, Western Australia Sheds New Light on the Development of Tessellated Calcified Cartilage. PloS one 10, e0126066.

Luo, G., Ducy, P., McKee, M. D., Pinero, G. J., Loyer, E., Behringer, R. R. & Karsenty, G. 1997. Spontaneous calcification of arteries and cartilage in mice lacking matrix GLA protein. Nature 386, 78–81.

Mahamid, J., Sharir, A., Gur, D., Zelzer, E., Addadi, L., Weiner, S., 2011. Bone mineralization proceeds through intracellular calcium phosphate loaded vesicles: A cryo-electron microscopy study. Journal of structural biology 174, 527–535.

Maisey, J.G., 2013. The diversity of tessellated calcification in modern and extinct chondrichthyans. Revue de Paleobiologie 32, 335–371.

Martin, R.B., Burr, D.B., Sharkey, N.A., Fyhrie, D.P., 2015. Skeletal Tissue Mechanics, 2nd ed. Springer New York, New York, NY.

McCarty, D.J., Hogan, J.M., Gatter, R.A., Grossman, M., 1966. Studies on pathological calcifications in human cartilage. I. Prevalence and types of crystal deposits in the menisci of two hundred fifteen cadavera. J Bone Joint Surg Am 48, 309–325.

Mollen, F.H., Wintner, S.P., Iglesias, S.P., 2012. Comparative morphology of rostral cartilages in extant mackerel sharks (Chondrichthyes, Lamniformes, Lamnidae) using CT scanning. Zootaxa 3340, 29–43.

Obrant, K.J., Odselius, R., 1985. Electron microprobe investigation of calcium and phosphorus concentration in human bone trabeculae—Both normal and in posttraumatic osteopenia. Calcif Tissue Int 37, 117–120.

Officer, R.A., Clement, J.G., Rowler, D.K., 1995. Vertebral deformities in a school shark, *Galeorhinus galeus*: circumstantial evidence for endoskeletal resorption? Journal of Fish Biology 46, 85–98.

Omelon, S., Georgiou, J., Variola, F., Dean, M.N., 2014. Colocation and role of polyphosphates and alkaline phosphatase in apatite biomineralization of elasmobranch tesserae. Acta Biomaterialia 10, 3899–3910.

Ortiz-Delgado, J. B., Simes, D. C., Viegas, C. S. B., Schaff, B. J., Sarasquete, C. & Cancela, M. L. (2005) Cloning of matrix Gla protein in a marine cartilaginous fish, *Prionace glauca*: preferential protein accumulation in skeletal and vascular systems. Histochemistry and Cell Biology 126**,** 89–101.

Peignoux-Deville, J., Lallier, F., Vidal, B., 1982. Evidence for the presence of osseous tissue in dogfish vertebrae. Cell Tissue Res 222, 605–614.

Penel, G., Leroy, N., Van Landuyt, P., Flautre, B., Hardouin, P., Lemaitre, J., & Leroy, G., 1999. Raman microspectrometry studies of brushite cement: in vivo evolution in a sheep model. Bone, 25, 81S-84S.

Porter, M.E., Beltran, J.L., Koob, T.J., Summers, A.P., 2006. Material properties and biochemical composition of mineralized vertebral cartilage in seven elasmobranch species (Chondrichthyes). Journal of Experimental Biology 209, 2920–2928.

Puchtler, H., Meloan, S.N., 1985. On the chemistry of formaldehyde fixation and its effects on immunohistochemical reactions. Histochemistry 82, 201–204.

Puchtler, H., Meloan, S.N., 1978. Demonstration of Phosphates in Calcium Deposits - Modification of Von Kossa Reaction. Histochemistry 56, 177–185.

Ravaglioli, A., Krajewski, A., Celotti, G.C., Piancastelli, A., Bacchini, B., Montanari, L., Zama, G., Piombi, L., 1996. Mineral evolution of bone. Biomaterials 17, 617–622.

Remaggi, F., Ferretti, M., Canè, V., Zaffe, D., 1996. Histomorphological and chemico-physical analyses of the mineral matrix of micropetrotic human bone. Ann. Anat. 178, 223–227.

Romeis, B., 1968. Mikroskopische Technik. Oldenbourg Verlag, München and Wien.

Seidel, R., Lyons, K., Blumer, M., Zaslansky,P., Fratzl, P., Weaver, J.C., Dean, M.N., 2016. Ultrastructural and developmental features of the tessellated endoskeleton of elasmobranchs (sharks and rays). Journal of Anatomy 229: 681-702.

Shellis, R.P., Heywood, B.R., Wahab, F.K., 1997. Formation of brushite, monetite and whitlockite during equilibration of human enamel with acid solutions at 37 degrees C. Caries Res. 31, 71–77.

Summers, A.P., 2000. Stiffening the stingray skeleton-an investigation of durophagy in myliobatid stingrays (Chondrichthyes, Batoidea, Myliobatidae). Journal of Morphology 243, 113–126.

Takagi, M., Parmley, R.T., Denys, F.R., Yagasaki, H., Toda, Y., 1984. Ultrastructural cytochemistry of proteoglycans associated with calcification of shark cartilage. The Anatomical Record 208, 149–158.

Temizel, N., Girisken, G., & Tas, A. C. 2011. Accelerated transformation of brushite to octacalcium phosphate in new biomineralization media between 36 C and 80 C. Materials Science and Engineering: C, 31, 1136-1143.

Urist, M.R., 1962. Calcium and other ions in blood and skeleton of Nicaraguan fresh-water shark. Science 137, 984–986.

Urist, M.R., 1961. Calcium and phosphorus in the blood and skeleton of the Elasmobranchii. Endocrinology 69, 778–801.

Verborgt, O., Gibson, G.J., Schaffler, M.B., 2000. Loss of Osteocyte Integrity in Association with Microdamage and Bone Remodeling After Fatigue In Vivo. Journal of Bone and Mineral Research 15, 60–67.

Ørvig, T., 1951. Ørvig T (1951) Histologic Studies of Placoderms and fossil Elasmobranchs. I: The endoskeleton, with remarks on the hard tissues of lower vertebrates in general. Arkiv för Zoologi 2, 321–454.